PEM fuel cell performance and its two-phase mass transport

Hong Sun[a], Hongtan Liu[a,b,*], Lie-Jin Guo[a]

[a] *State Key Laboratory of Multiphase Flow in Power Engineering, Xi'an Jiaotong University, Xi'an, Shanxi 710049, PR China*
[b] *Department of Mechanical Engineering, University of Miami, Coral Gables, FL 33124, USA*

Abstract

A two-phase flow model for a proton exchange membrane (PEM) fuel cell is developed. The model is based on the mixture flow model and the unified approach is used. Instead of using a separate model for the catalyst layer, the catalyst layers are now included in the respective unified domains for the cathode and anode, thus continuity boundary conditions at the interface between the catalyst layer (CL) and the gas diffuser layer (GDL) are no longer needed. The model couples the flows, species, electrical potential, and current density distributions in the cathode and anode fluid channels, gas diffusers, catalyst layers and membrane respectively. Furthermore, the two-phase flow model is also used in the anode side, and the momentum transfer between the liquid and gas phases due to phase change is taken into consideration. Experiments have been conducted to study the performances of a PEM fuel cell and the results are used to improve and validate our model. The modeling results of polarization curves compared well with the experimental data. The model is used to study the influences of fuel cell operating temperature, operating pressure and humidification temperature on the oxygen, vapor and liquid water transports, as well as fuel cell performances.
© 2004 Elsevier B.V. All rights reserved.

Keywords: Proton exchange membrane (PEM); Fuel cells; Two-phase flow; Water management

1. Introduction

It is well known that water management is a critical issue in proton exchange membrane (PEM) fuel cell design and operations. On one hand, the polymer membrane in PEM fuel cells needs to be hydrated to maintain high proton conductivity. On the other hand, excessive liquid water may occupy a significant fraction of the pore volume in the catalyst layer and gas diffusion layer (GDL), thus may significantly reduce reactant transfer rate to the reaction sites and cause flooding. Therefore, proper water balance and management is essential to maintaining high performance of a PEM fuel cell. A good understanding and proper modeling of the various transport processes, especially water transport is essential for the improvement and optimization of a fuel cell and fuel cell sys-

tems. At present many of the transport phenomena inside a fuel cell cannot be directly observed or measured; thus making mathematical modeling a critical tool to understanding these transport phenomena.

Some of the pioneering work in PEM fuel cell modeling includes those by Bernardi and Verbrugge [1,2], Hill and Verbrugge [3], Springer et al. [4,5]. These one-dimensional models laid the foundation for PEM fuel cell modeling. Pseudo two-dimensional model includes those by Fuller and Newman [6] and Nguyen and White [7], which included the effects of reactant consumption along the flow channels. Gurau et al. [8] developed a two-dimensional PEM fuel cell model that coupled fluid flow, mass transfer and the electrokinetics, thus introducing the computational fluid dynamics (CFD) into fuel cell modeling. The approach adopted was a unified approach that eliminated the need of prescribing artificial boundary conditions at the various interfaces between the different components of a fuel cell. Zhou and Liu [9]

Nomenclature

a	catalyst surface area per unit volume ($cm^2\,cm^{-3}$)
C	species mass fraction
D	diffusion coefficient ($cm^2\,s^{-1}$)
E	potential (V)
E_m	Equivalent weight of ionomer ($g\,(equiv.)^{-1}$)
f_e	surface area of liquid water per unit volume
F	Faraday constant ($96487\,C\,mol^{-2}$)
i_0	exchange current density ($A\,cm^{-2}$)
I	current density ($A\,cm^{-2}$)
$J(s)$	capillary pressure function
k_r	relative permeability
K	absolute permeability (cm^2)
L	characteristic size (cm)
M	molecular weight ($kg\,mol^{-1}$)
N	mole flux ($kg\,cm^{-2}\,s^{-1}$)
p	pressure (Pa)
R	universal gas constant ($8.314\,J\,mol^{-1}\,K^{-1}$)
s	phase saturation
Sh	Sherwood number
T	temperature
$\mathbf{u}$	velocity vector ($cm\,s^{-1}$)
u	the x direction velocity component ($cm\,s^{-1}$)
v	the y direction velocity component ($cm\,s^{-1}$)
x	mole fraction

Greek symbols

α	net water transport coefficient
α_a	anodic transfer coefficient
α_c	cathodic transfer coefficient
γ	multiphase correction factor
δ	width (mm)
ε	porosity
η	overpotential (V)
λ	water content in membrane or individual mobility
μ	viscosity ($N\,s\,cm^{-2}$)
ν	kinematic viscosity ($cm^2\,s^{-1}$)
ρ	density ($kg\,m^{-3}$)
σ	interfacial tension ($N\,cm^{-1}$)

Subscripts and superscripts

a	anode or air
act	activity
c	cathode or capillary
d	electro-osmotic drag
diff	diffusion
eff	effective
g	gas phase
hyd	hydraulic
in	inlet
k	phase k
l	liquid phase
m	membrane or mixture
r	relative
s	solid
sat	saturation
v	vapor
w	water
α	species

and Um and Wang [10] developed three-dimensional models using a similar approach by Gurau et al. [8].

Wang et al. [11] and You and Liu [12] developed PEM fuel cell models that applied two-phase flow model for the cathode side of the PEM fuel cell. The model by Wang et al. [11] treated the cathode catalyst layer as an surface and did not included the membrane and the anode side; while the model by You and Liu [12] treated the cathode catalyst layer separately by a pseudo-homogenous model [13] and only single-phase flow model was used at the anode side.

In this study, we developed a two-phase flow model using a similar treatment as in You and Liu [12] and Wang et al. [11], but our model treated the catalyst layers as integral parts of the unified domains, where the electrochemical reactions are incorporated as source terms. This approach eliminated the necessity of prescribing interfacial boundary conditions between the catalyst layer and the GDL. Now the two-phase flow model is also applied to the anode side and the two gas channels. In addition, the momentum transfer between the liquid and gas phases due to phase change is taken into consideration.

2. Experimental system

A flow diagram of the experimental system is shown in Fig. 1. The fuel cell test system can control the reactant gas flow rates, fuel cell operating temperature, reactant gas humidification temperature and operating pressure. The reactant gas flow rates are regulated by two mass flow controllers; the humidification temperatures of the reactant gases are controlled by regulating the humidifier temperature; and the operating pressures are regulated by adjusting the back pressure regulators. A nitrogen purging system is incorporated in the experimental system to purge both the anode and cathode sides before and after experiments to ensure safety. Experimental data are recorded after the fuel cell operation reaches steady state.

In this study, a single PEM fuel cell with an active area of $5\,cm^2$ was used. The membrane used was Nafion™ 117 membrane, the gas diffusion layers (GDLs) were carbon fiber paper, and the carbon supported platinum with a loading of $0.4\,mg\,cm^{-2}$ was used on both the anode and cathode sides. The collector plates were made of carbon and the flow fields
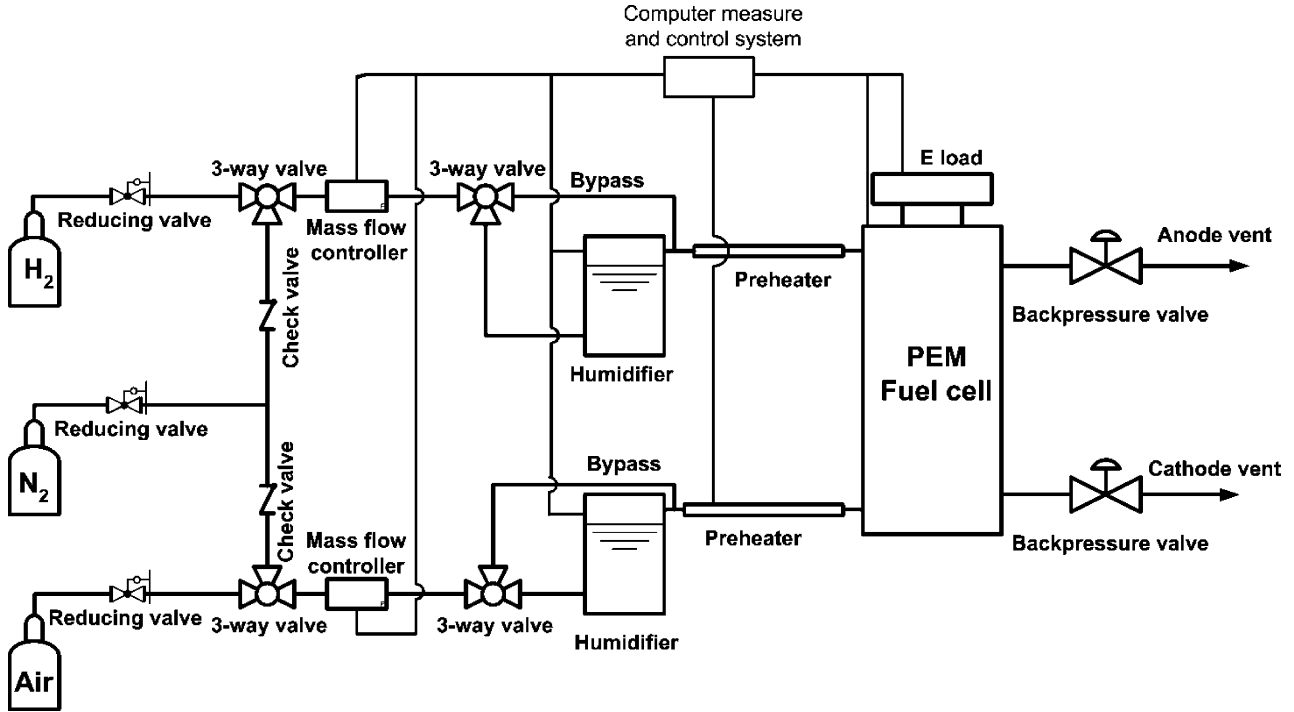
Fig. 1. The schematic of the fuel cell experimental system.

are serpentine on both sides. The end plates were made of copper. Detailed information of the fuel cell used is listed in Table 1.

3. Mathematical model

As stated earlier, the flow model used is the mixture two-phase flow model [14,15], and we used the two-phase flow model in both the cathode and anode sides, including the two gas channels. The catalyst layers are also included in the unified domains of cathode and anode, and the same two-phase flow model is applied. In addition, the momentum transfer between the liquid and gas phases due to phase change is taken into consideration.

The modeling domains of a PEM fuel cell are shown in Fig. 2. Three different domains are considered, one for the cathode fluid, one for the anode fluid, and one for water. The cathode and anode domains each consist of the respective gas channel, GDL and catalyst layer (CL), and the domain

Table 1
Geometric parameters and catalyst loading of the experimental fuel cell

Active area (cm^2)	5.0
Channel length (cm)	2.24
Channel width (cm)	0.1
Channel depth (cm)	0.09
Gas diffuser thickness (cm)	0.03
Catalyst layer thickness (cm)	0.00129
Membrane thickness (cm)	0.0108
The anode and cathode CTL loading (mg)	0.4

for water include all the components: two gas channels, two GDLs, two catalyst layers and the membrane.

3.1. Continuity equation

The continuity equation for the two-phase mixture is:

$$\frac{\partial(\varepsilon\rho)}{\partial t} + \nabla(\varepsilon\rho u) = 0 \tag{1}$$

where ε is the porosity and it equals one in the channels if the liquid volume fraction is zero.

3.2. Momentum equations

The momentum equations for the liquid water and the gas mixtures in both anode and cathode are respectively:

$$\frac{\partial(\varepsilon\rho u_l)}{\partial t} + \nabla(\varepsilon_l \rho_l u_l u_l) + \dot{m}(u_l - u_g)$$

$$= \nabla(\varepsilon_l \mu_l \nabla u_l) + \begin{cases} 0 & \text{gas channel} \\ -\dfrac{\mu_l}{K_l}(\varepsilon_l^2 u_l) & \text{GDL and CL} \end{cases} \tag{2}$$

$$\frac{\partial(\varepsilon\rho u_g)}{\partial t} + \nabla(\varepsilon_g \rho_g u_g u_g) + \dot{m}(u_g - u_l)$$

$$= -\varepsilon_g \nabla P + \nabla(\varepsilon_g \mu_g \nabla u_g)$$

$$+ \begin{cases} 0 & \text{gas channel} \\ -\dfrac{\mu_g}{K_g}(\varepsilon_g^2 u_g) & \text{GDL and CL} \end{cases} \tag{3}$$
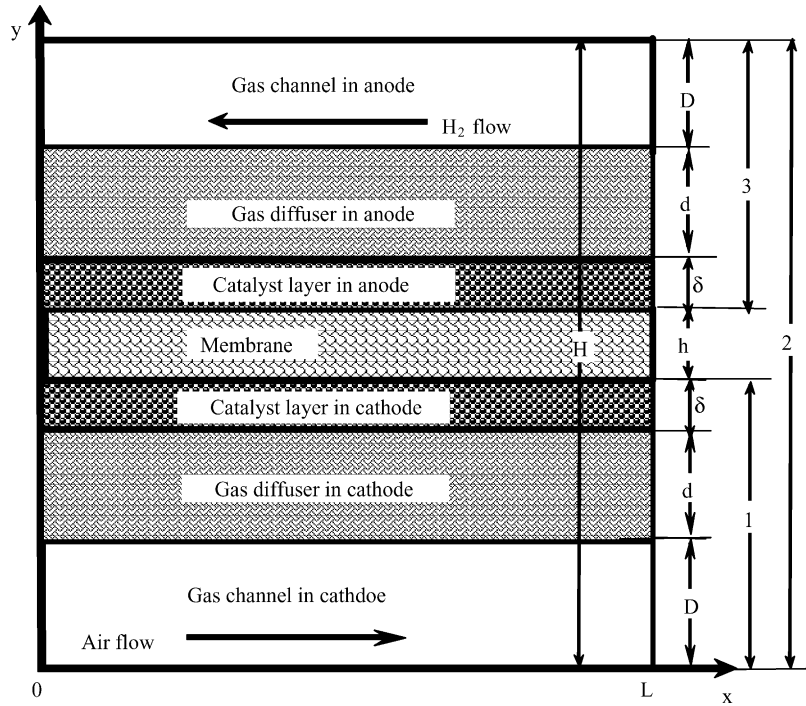
where $\dot{m}$ is the rate of phase change.

Fig. 2. The unified modeling domains. (1) Domain for cathode fluid; (2) domain for water; (3) domain for the anode fluid. (L) channel length; (D) channel depth; (d) gas diffuser thickness; (δ) catalyst layer thickness; (h) membrane thickness.

3.3. Water transport equation in membrane

The governing equation for liquid water transfer in the membrane is given by [6]:

$$N_w^{net} = \frac{n_d I}{F} - D_w \frac{dC_w}{dy} - C_w \frac{K_m}{\mu} \frac{dP_w}{dy} \tag{4}$$

3.4. Species conservation

The species conservation equation is given by [14,15]:

$$\frac{\partial(\varepsilon \rho C)}{\partial t} + \nabla(\gamma_\alpha \rho u C^\alpha) = \nabla(\varepsilon \rho D \nabla C^\alpha)$$
$$+ \nabla \left[\varepsilon \sum_k [\rho_k s_k D_k^\alpha (\nabla C_k^\alpha - \nabla C^\alpha)] \right] - \nabla \left[\sum_k C_k^\alpha N_k \right] \tag{5}$$

where k denotes either gas phase or liquid phase, α indicates species, such as oxygen, nitrogen or water in the cathode, and it indicates hydrogen or water in the anode, and γ_α is the correction factor to be given below.

3.5. Mixture properties and parameters

The properties and parameters for the mixture are given below:

$$\text{Density}: \quad \rho = \rho_l s + \rho_g(1 - s) \tag{6}$$

$$\text{Concentration}: \quad \rho C^\alpha = \rho_l C_l^\alpha s + \rho_g C_g^\alpha (1 - s) \tag{7}$$

$$\text{Velocity}: \quad \rho u = \rho_l u_l + \rho_g u_g \tag{8}$$

$$\text{Diffusion coefficient}: \quad \rho D^\alpha = \rho_l s D_l^\alpha + \rho_g(1 - s)D_g^\alpha \tag{9}$$

$$\text{Correction factor}: \quad \gamma_\alpha = \frac{\rho(\lambda_l C_l^\alpha + \lambda_g C_g^\alpha)}{\rho_l s C_l^\alpha + \rho_g(1 - s)C_g^\alpha} \tag{10}$$

$$\text{Relative mobility}: \quad \lambda_l = \frac{k_{rl}/\nu_l}{k_{rl}/\nu_l + k_{rg}/\nu_g} \tag{11}$$

$$\lambda_g = 1 - \lambda_l \tag{12}$$

$$\text{Fluid kinematics viscosity}: \quad \nu = \frac{1}{k_{rl}/\nu_l + k_{rg}/\nu_g} \tag{13}$$

$$\text{Porosity}: \quad \varepsilon = \varepsilon_l + \varepsilon_g \tag{14}$$

where $\varepsilon_l = s\varepsilon$ representing the volume fraction of liquid water in the porous media, $\varepsilon_g = (1 - s)\varepsilon$ is the effective porosity that denotes the volume fraction of the gas mixture in the porous media, and s is the liquid saturation, representing the volume fraction of liquid water in the pores.

In addition to the above equations, the multiphase mixture model incorporates some important relations for determining the velocities of individual phases in the mixture flow field:

$$\varepsilon \rho_l u_l = N_l + \lambda_l \varepsilon \rho u \tag{15}$$

$$\varepsilon \rho_g u_g = -N_l + \lambda_g \varepsilon \rho u \tag{16}$$

$$N_l = K \frac{\lambda_l \lambda_g}{\nu} \nabla P_C \tag{17}$$

$$N_g + N_l = 0 \tag{18}$$

3.6. Constitutive relations

The porous electrode is treated as homogeneous porous media. The empirical correlations for the relative permeabilities for the liquid and gas phases are respectively [15]:

$$k_{rl} = s^3 \tag{19}$$

$$k_{rg} = (1 - s)^3 \tag{20}$$

The capillary pressure is considered as a function of saturation and the empirical equation is [14]:

$$P_C = P_g - P_l = \sigma \left(\frac{\varepsilon}{K} \right)^{1/2} J(s) \tag{21}$$

where $J(s_l)$ is the Leverett function given by [16]:

$$J(s) = 1.417(1 - s) - 2.120(1 - s)^2 + 1.263(1 - s)^3 \tag{22}$$

The rate of phase change is given by [17]:

$$\dot{m} = Sh \frac{D_v^{eff}}{L} f_e \frac{PM_v}{RT} \left(\frac{P_{sat}}{P} - x_v \right) \tag{23}$$

where Sh is the Sherwood number, x_v the mole fraction of water vapor, P the pressure of the gas mixture, and M_v the molecular weight of water vapor.

The saturation vapor pressure is given by [6]:

$$\log_{10} P_{sat} = -2.1794 + 0.02953T - 9.1837 \times 10^{-5} T^2$$
$$+ 1.4454 \times 10^{-7} T^3 \tag{24}$$

The liquid water saturation s, representing the volumetric fraction of void space occupied by the liquid water, is given by [15]:

$$s = \frac{\rho C^{H_2O} - \rho_g C_g^{H_2O}}{\rho_l - \rho_g C_g^{H_2O}} \tag{25}$$

The Butler–Volmer equation is used to model the electrochemical reaction rates in the catalyst layers

$$j = ai_0 \left(\frac{C_R}{C_R^{ref}} \right)^k \left[\exp \left(\frac{\alpha_a F\eta}{RT} \right) - \exp \left(\frac{-\alpha_c F\eta}{RT} \right) \right] \tag{26}$$

where R is oxygen or hydrogen; k equals 1 for the cathode side and 0.5 for the anode side.

3.7. Relationships for the membrane

Water may transport through the membrane under three different transport mechanisms: electro-osmotic drag, back diffusion and hydraulic permeation. A net water transport coefficient is defined as [e.g. You and Liu]

$$\alpha = 2.5 \frac{\lambda}{22} - D_w \frac{F}{I} \frac{dC_w}{dy} - C_w \frac{K_m}{\mu} \frac{F}{I} \frac{dP_w}{dy} \tag{27}$$

The water diffusion flux in membrane is

$$N_w^{diff} = -D_w \frac{dC_w}{dy_{m,w}} \tag{28}$$

Water molar concentration in membrane is given by [18]

$$C_w = \frac{\rho_{m,d} \rho_w \lambda}{\rho_{m,d} M_w \lambda + \rho_w E_m} \tag{29}$$

Water content in membrane can be determined by water activity.

$$\lambda = \begin{cases} 0.043 + 17.81a - 39.85a^2 + 36.0a^3 & 0 < a = \frac{x_w P}{P_{sat}} \leq 1 \\ 14 + 1.4 \left(\frac{x_w P}{P_{sat}} - 1 \right) & 1 < a = \frac{x_w P}{P_{sat}} \leq 3 \\ 22 & a = \frac{x_w P}{P_{sat}} > 3 \end{cases} \tag{30}$$

The water diffusion coefficient in the membrane can be expressed as [18]:

$$D_w = (11.102 + 9.129(1 - \exp(-0.108\lambda)))$$
$$\left[\frac{E_m}{R} \left(\frac{1}{303} - \frac{1}{T} \right) \right] \tag{31}$$

The ionic conductivity is [18]:

$$\kappa = (-4.43 + 0.0179T)(-0.0108 + 0.2365$$
$$\times (1 - \exp(-0.0285\lambda))) \tag{32}$$

The membrane resistance is determined by integrating the resistance over the membrane thickness. Taking into the effect of membrane swell, it is given by:

$$AR_m = \int_0^H \frac{(c_d \lambda + 1)^{1/3} \, dy_d}{\kappa} \tag{33}$$

where

$$c_d = \frac{\rho_{m,d} M_w}{\rho_w E_m} \tag{34}$$

3.8. Boundary conditions

Boundary conditions are required to solve the continuity, momentum and species conservation equations. At the

inlet of the anode and the cathode, the fluids have given velocities. The standard exit boundary and no-slip boundary conditions are used at the channel exits and channel walls. In the species field, the inlet species concentrations are prescribed, the species gradients are set to zero at the channel exits and at the walls. The gradients of reactant (oxygen or hydrogen) concentrations are assumed to be zero at the interface between the membrane and the respective catalyst layer. The detailed boundary conditions are given below.

At the cathode inlet ($x = 0$)

$$u|_{x=0} = u_{\text{in}}, \qquad v|_{x=0} = 0, \qquad C^{\text{H}_2\text{O}}\big|_{x=0} = \frac{\rho_{\text{g,sat}}^{\text{H}_2\text{O}}\, \text{RH}_{\text{in}}^{\text{a}}}{\rho_{\text{g}}},$$

$$C^{\text{O}_2}\big|_{x=0} = C_{\text{in}}^{\text{O}_2}, \qquad 0 \le y < D \tag{35}$$

where $\text{RH}_{\text{in}}^{\text{a}}$ is relative humidify of inlet air.

$$u|_{x=0} = 0, \qquad v|_{x=0} = 0,$$

$$\frac{\partial C^{\text{H}_2\text{O}}}{\partial x}\bigg|_{x=0} = 0, \qquad \frac{\partial C^{\text{O}_2}}{\partial x}\bigg|_{x=0} = 0, \qquad D \le y \le D + d + \delta \tag{36}$$

At the cathode outlet ($x = L$)

$$\frac{\partial u}{\partial x}\bigg|_{x=L} = 0, \qquad \frac{\partial C^{\text{H}_2\text{O}}}{\partial x}\bigg|_{x=L} = 0, \qquad \frac{\partial C^{\text{O}_2}}{\partial x}\bigg|_{x=L} = 0,$$

$$v|_{x=L} = 0, \qquad 0 \le y < D \tag{37}$$

$$u|_{x=L} = 0, \qquad v|_{x=L} = 0, \qquad \frac{\partial C^{\text{H}_2\text{O}}}{\partial x}\bigg|_{x=L} = 0,$$

$$\frac{\partial C^{\text{O}_2}}{\partial x}\bigg|_{x=L} = 0, \qquad D \le y \le D + d + \delta \tag{38}$$

At the wall of the cathode channel ($y = 0$)

$$u|_{y=0} = 0, \qquad v|_{y=0} = 0,$$

$$\frac{\partial C^{\text{H}_2\text{O}}}{\partial y}\bigg|_{y=0} = 0, \qquad \frac{\partial C^{\text{O}_2}}{\partial y}\bigg|_{y=0} = 0, \qquad 0 \le x \le L \tag{39}$$

At the interface between the membrane and the cathode catalyst layer

$$\frac{\partial C^{\text{O}_2}}{\partial y}\bigg|_{y=D+d+\delta} = 0, \qquad 0 \le x \le L \tag{40}$$

At the anode inlet ($x = L$)

$$u|_{x=L} = u_{\text{H}_2,\text{in}}, \qquad v|_{x=L} = 0,$$

$$C^{\text{H}_2\text{O}}\big|_{x=L} = \frac{\rho_{\text{g,sat}}^{\text{H}_2\text{O}}\, \text{RH}_{\text{in}}^{\text{H}_2}}{\rho_{\text{g}}}, \qquad C^{\text{H}_2}\big|_{x=L} = C_{\text{in}}^{\text{H}_2},$$

$$D + 2d + 2\delta + h \le y < H \tag{41}$$

where $\text{RH}_{\text{in}}^{\text{H}_2}$ is relative humidify of the anode inlet gas.

$$u|_{x=L} = 0, \qquad v|_{x=L} = 0, \qquad \frac{\partial C^{\text{H}_2\text{O}}}{\partial x}\bigg|_{x=L} = 0,$$

$$\frac{\partial C^{\text{H}_2}}{\partial x}\bigg|_{x=L} = 0, \qquad D + d + \delta + h \le y \le D + 2d + 2\delta + h \tag{42}$$

At the anode outlet ($x = 0$)

$$\frac{\partial u}{\partial x}\bigg|_{x=0} = 0, \qquad \frac{\partial C^{\text{H}_2\text{O}}}{\partial x}\bigg|_{x=0} = 0, \qquad \frac{\partial C^{\text{H}_2}}{\partial x}\bigg|_{x=0} = 0,$$

$$v|_{x=0} = 0, \qquad D + 2d + 2\delta + h \le y < H \tag{43}$$

$$u|_{x=0} = 0, \qquad v|_{x=0} = 0, \qquad \frac{\partial C^{\text{H}_2\text{O}}}{\partial x}\bigg|_{x=0} = 0,$$

$$\frac{\partial C^{\text{H}_2}}{\partial x}\bigg|_{x=0} = 0, \qquad D + d + \delta + h \le y \le D + 2d + 2\delta + h \tag{44}$$

At the wall of the anode channel ($y = H$)

$$u|_{y=H} = 0, \qquad v|_{y=H} = 0, \qquad \frac{\partial C^{\text{H}_2\text{O}}}{\partial y}\bigg|_{y=H} = 0,$$

$$\frac{\partial C^{\text{H}_2}}{\partial y}\bigg|_{y=H} = 0, \qquad 0 \le x \le L \tag{45}$$

At the interface between the membrane and the anode catalyst layer:

$$\frac{\partial C^{\text{H}_2}}{\partial y}\bigg|_{y=D+d+\delta+h} = 0, \qquad 0 \le x \le L \tag{46}$$

4. Results and discussion

The governing equations with the boundary conditions are solved numerically by a finite-volume method. Table 2

Table 2
The parameters used in the model for the base case

Gas diffuser porosity	0.4
Gas diffuser tortuosity	1.5
Catalyst layer porosity	0.25
Air stoic ratio	3.5
Hydrogen stoic ratio	2
Catalyst surface area ($\text{cm}^2\,\text{cm}^{-3}$)	1.4×10^5
Exchange current density ($\text{A}\,\text{cm}^{-2}$)	4.84×10^{-8}
Cathodic transfer coefficient	0.52
Anodic transfer coefficient	0.54
Dry membrane density ($\text{kg}\,\text{m}^{-3}$)	2.16
Ionomer equivalent weight	1100
$Sh\, f_e/L$ (cm^{-2})	20000

lists the parameters used in the base case, and the geometric parameters are listed in Table 1.

4.1. The effect of fuel cell operating temperature

It is well know that operating temperature has a significant effect on fuel cell performances. The activation energy decreases with temperature and various transport properties, such as membrane proton resistance, gas diffusivities, etc. all depends on temperature. Fig. 3 shows the modeling results of a fuel cell performance at different temperatures compared with experimental data. The humidification temperatures on both the anode and cathode sides are 70 °C, the operating pressures are 3 atm on both sides, and the flow rates are 100 sccm on the anode side and 200 sccm on the cathode side. Within the parameter range, the performance of the fuel cell increases with temperature and the modeling results agree well with experimental data except at high current density, where the model over-predicts fuel cell performance.

Figs. 4 and 5 show the oxygen mass fraction distributions in the cathode catalyst layer at the same overpotential for two different operating temperatures of 70 and 80 °C, respectively. The average cell current densities corresponding Figs. 4 and 5 are 0.926 and 1.082 A cm^{-2} respectively. At the same overpotential, the cell generates higher current at higher cell temperature, and more current is generated in the region close to the GDL (low value of y/δ) and lower oxygen concentration is found in the region near the membrane (high value of y/δ). This is due to the fact that at higher temperatures, the chemical reaction occurs more readily and more oxygen is consumed before reaching the deeper region of the catalyst layer. This indicates that at higher operating temperature the effective thickness of the catalyst layer [13] is thinner and this result should be taken into consideration in catalyst layer design and optimization.
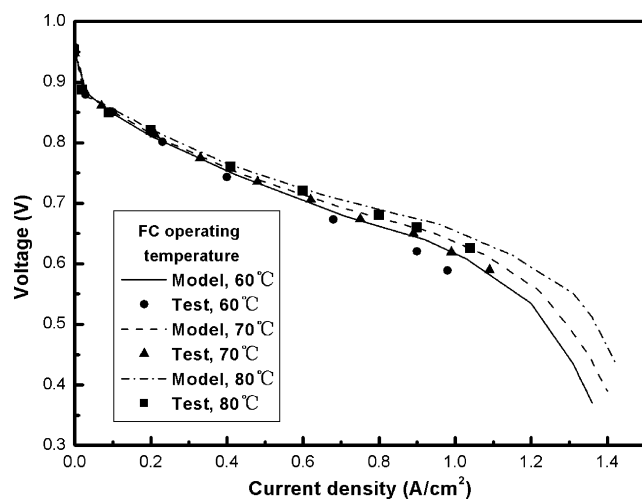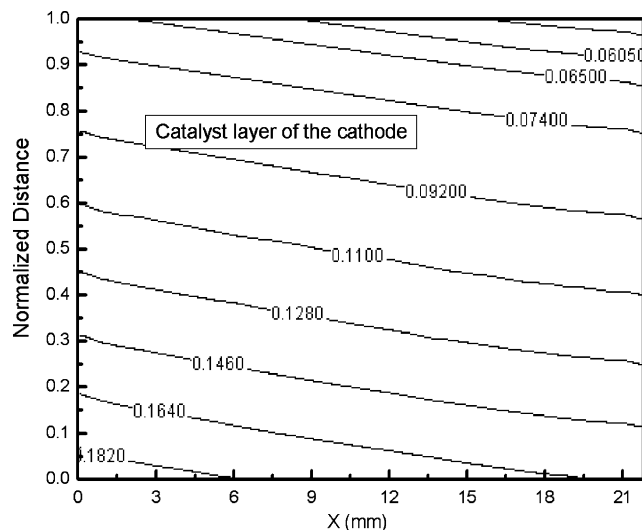

Fig. 4. Oxygen mass fractions in the cathode catalyst layer at fuel cell operating temperature of 70 °C. Normalized distance is from the cathode catalyst layer's interface with GDL to its interface with the membrane. Case conditions: H$_2$ flow rate = 100 sccm, humidification temperature on both sides = 60 °C, pressure on both sides = 3 atm; air flow rate = 200 sccm.

Figs. 6 and 7 show the total water mass fraction distributions across the cathode catalyst layer at different locations along the flow direction for two different operating temperatures of 70 and 80 °C, respectively. Total water mass fraction increases along the flow direction due to the accumulation of water produced in the catalyst layer and the electro-osmotic drag from anode. Total water mass fractions are generally higher for the higher temperature case (Fig. 7). This can be attributed to the higher water production rate and higher rate of electro-osmosis due to higher current densities.

Fig. 3. Comparison of the modeling results with experimental data at different fuel cell operating temperatures. Case conditions: H$_2$ flow rate = 100 sccm, humidification temperature on both sides = 70 °C, operating pressure = 3 atm on both sides; air flow rate = 200 sccm.
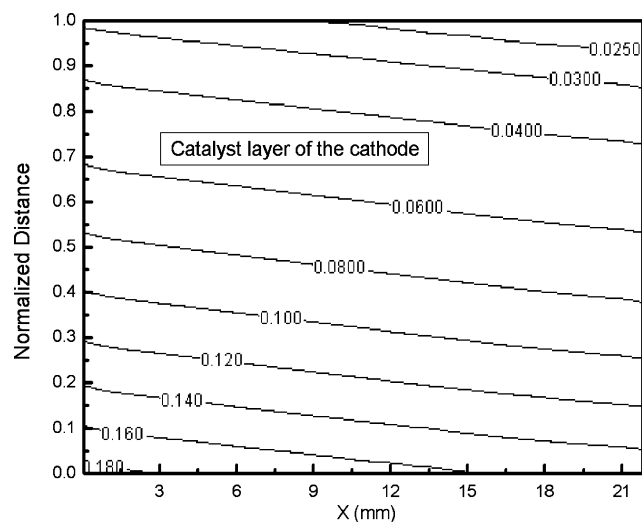

Fig. 5. Oxygen mass fraction in the cathode catalyst layer for fuel cell temperature = 80 °C. Normalized distance is from the cathode catalyst layer's interface with GDL to its interface with the membrane. Case conditions: H$_2$ flow rate = 100 sccm, humidification temperature on both sides = 60 °C, pressure on both sides = 3 atm; air flow rate = 200 sccm.
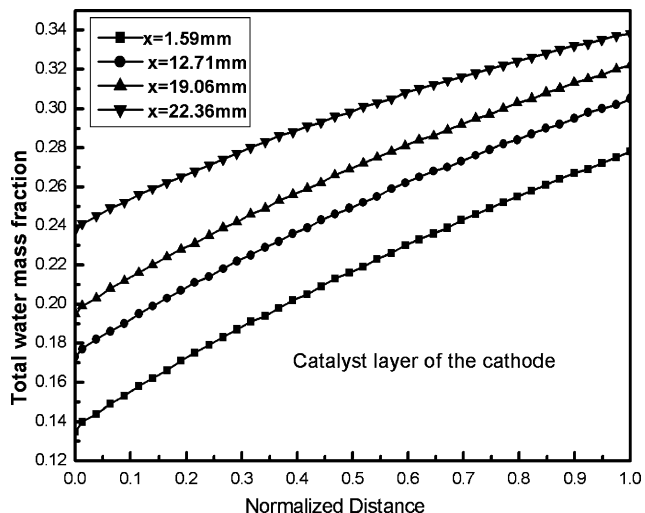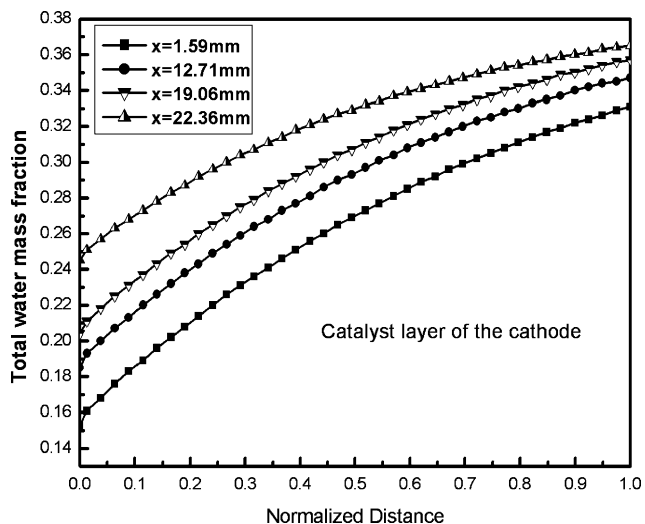
Fig. 6. Total water mass fractions at different cross sections in the cathode catalyst layer. Normalized distance is from the cathode catalyst layer's interface with GDL to its interface with the membrane. Case conditions: H_2 flow rate = 100 sccm, humidification temperature on both sides = 60 °C, pressure on both sides = 3 atm; air flow rate = 200 sccm. Fuel cell temperature = 70 °C.
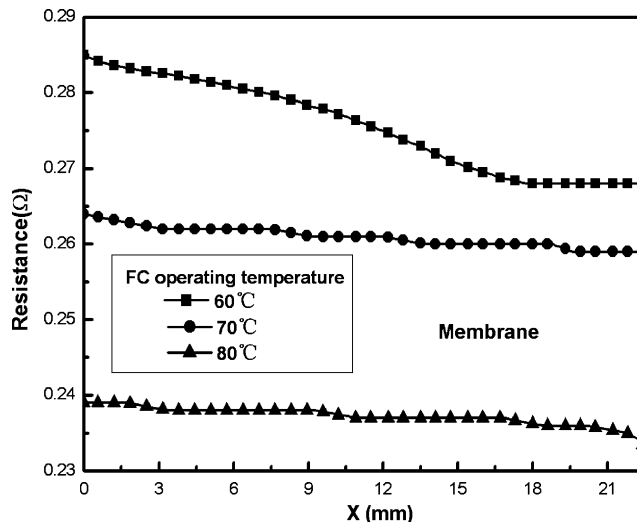

Fig. 8. Resistance in the membrane with different fuel cell operating temperatures. X is the flow direction and $X = 0$ is the inlet. Case conditions: H_2 flow rate = 100 sccm, humidification temperature on both sides = 60 °C, pressure on both sides = 3 atm; air flow rate = 200 sccm.

It is shown in Fig. 8 that the resistance in the membrane for the fuel cell operating temperature at 80 °C is lower than that at 60 and 70 °C. At a higher operating temperature, the electrochemical reaction is faster, and more water is produced in the cathode. More water makes the membrane better hydrated, and thus ionic resistance is reduced. Fig. 8 shows that for operating temperature at 60 °C, resistance in the membrane decreases along the flow direction. This indicates that there is more water in membrane near the outlet than that near the inlet.

Fig. 9 shows water content distributions across the membrane at different locations along the channel. Water content in membrane increases from anode side to cathode side due to electro-osmosis and water generation in the cathode. It is clear from Fig. 9 that the average water content near the cathode outlet is higher than that near the inlet. This is caused by water accumulation along the channel and leads to a lower ionic resistance near the outlet.

Fig. 7. Total water mass fractions at different cross sections in the cathode catalyst layer. Normalized distance is from the cathode catalyst layer's interface with GDL to its interface with the membrane. Case conditions: H_2 flow rate = 100 sccm, humidification temperature on both sides = 60 °C, pressure on both sides = 3 atm; air flow rate = 200 sccm, fuel cell temperature = 80 °C.
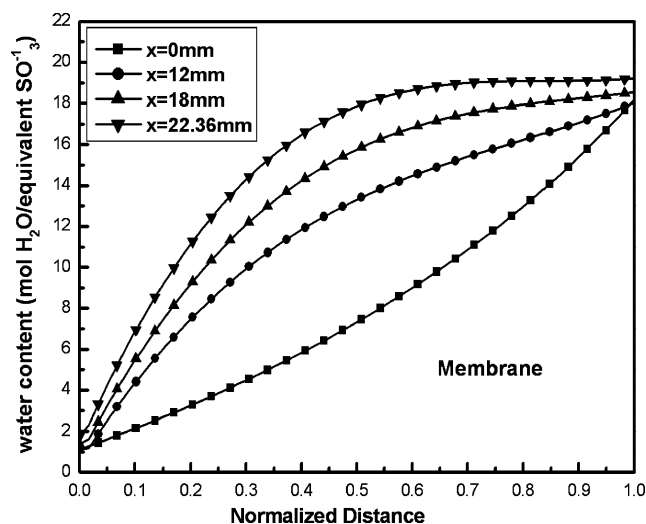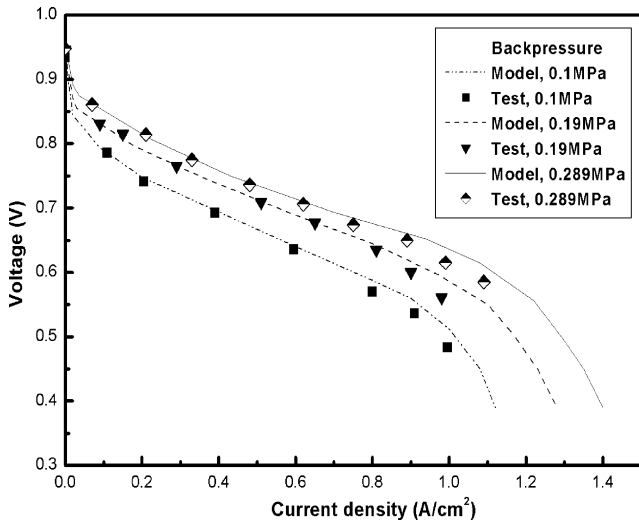

Fig. 9. Water content at different cross sections in the membrane. Normalized distance is from the membrane's interface with the anode CL to the interface with the cathode CL. Case conditions: H_2 flow rate = 100 sccm, humidification temperature on both sides = 60 °C, pressure on both sides = 3 atm; air flow rate = 200 sccm, fuel cell temperature = 60 °C.

Fig. 10. Performance comparisons between modeling results and experimental data at different operating pressures. Case conditions: H_2 flow rate = 100 sccm, humidification temperature on both sides = 70 °C; air flow rate = 200 sccm, fuel cell temperature = 70 °C.

4.2. The effect of operating pressure

Operating pressure is also an important parameter for PEM fuel cell. Fig. 10 shows the comparison of modeling prediction of a fuel cell performance at different operating pressures with the experimental results. The fuel cell operating temperature and humidification temperature on both the anode and cathode sides are 70 °C. Inlet flow rates are 100 sccm on the anode side and 200 sccm on the cathode side. It is shown in Fig. 10 that modeling results agree well with the experimental results, and fuel cell performances increases with operating pressure.

Fig. 11 shows the oxygen mass fraction in the cathode catalyst layer for operating pressure at 2 atm. A comparison of Figs. 5 and 11 clearly shows that oxygen mass fraction in Fig. 11 (lower pressure) is higher than that in Fig. 5 (higher pressure), and the gradient of oxygen mass fraction is lower in the lower pressure case (Fig. 11). At a higher operating pressure, the electrochemical reaction rate is higher and the current density is higher, thus more oxygen is consumed in cathode catalyst layer. This leads to lower oxygen concentration and greater oxygen gradient in the catalyst layer.

Fig. 12 shows the total water mass fraction at different cross sections in the cathode catalyst layer at the operating pressure of 2 atm. Comparing Fig. 12 with Fig. 7, one can see that total water mass fraction in the cathode catalyst layer for a lower operating pressure (Fig. 12) is lower. This can be attributed to the lower water generation rate and the lower electro-osmosis due to the lower current density.

Fig. 13 shows the variation of liquid water saturation across the cathode channel and GDL at different operating pressures. It is clear that liquid water saturation increases with operating pressure. Liquid water appears when the water vapor partial pressure exceeds the local water saturation
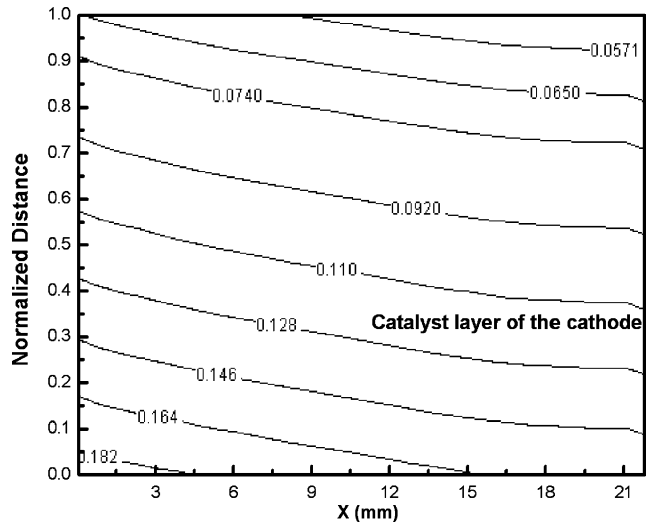

Fig. 11. Oxygen mass fractions in the cathode catalyst layer with operating pressure at 2 atm. Normalized distance is from the cathode catalyst layer's interface with GDL to the interface with the membrane. Case conditions: H_2 flow rate = 100 sccm, humidification temperature on both sides = 60 °C, pressure on both sides = 2 atm; air flow rate = 200 sccm, fuel cell temperature = 80 °C.

pressure. At a higher pressure, the vapor faction in the gas stream is lower and more water exists in liquid form. Besides, at a higher operating pressure, the fuel cell current density is higher and more water is produced. It is also shows in Fig. 13 that the liquid water saturation in the GDL is larger than that in the gas channel.

4.3. The effect of humidification temperature

Humidity of input gas is another very important parameter for PEM fuel cell operations. For most humid-
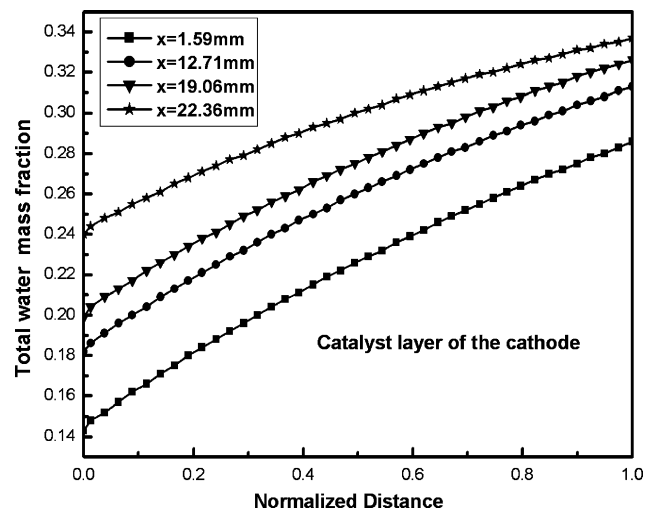

Fig. 12. Total water mass fractions at different cross sections in the cathode catalyst layer. Normalized distance is from the cathode catalyst layer's interface with GDL to the interface with the membrane. Case conditions: H_2 flow rate = 100 sccm, humidification temperature on both sides = 60 °C, pressure on both sides = 2 atm; air flow rate = 200 sccm, fuel cell temperature = 80 °C.
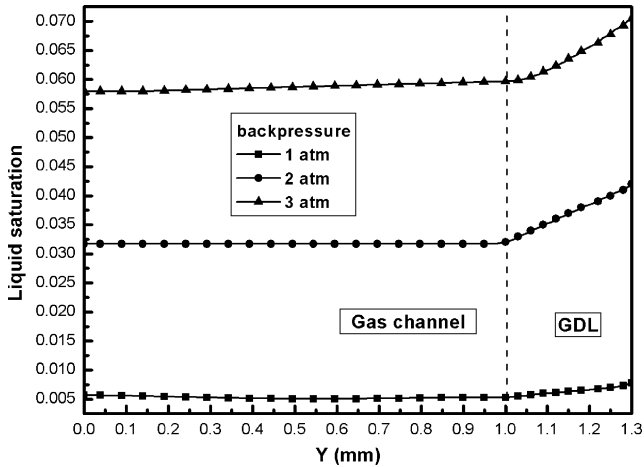
Fig. 13. Liquid saturation at $x = 22.36$ mm in the cathode with different operating pressures. The coordinate y starts at the channel wall (see Fig. 2). Case conditions: H_2 flow rate = 100 sccm, humidification temperature on both sides = 80 °C; air flow rate = 200 sccm, fuel cell temperature = 80 °C.

ifiers, humidity is regulated by controlling the temperature.

Fig. 14 shows the liquid water saturation in the cathode at different humidification temperatures. The humidification temperatures on the anode side for each case equal that on the cathode side. It is seen from Fig. 14 that the liquid water saturation increases with the gas stream humidification temperature. This is an obvious result, since more water vapor enters the fuel cell at higher humidification temperatures.

Fig. 15 shows the total water mass fraction at the interface between the anode GDL catalyst layer at three different humidification temperatures. Note that the anode flow is in the opposite direction to that of the cathode due to the counter-flow arrangement. Under this low hydrogen flow rate, along the anode flow direction, total water mass fraction
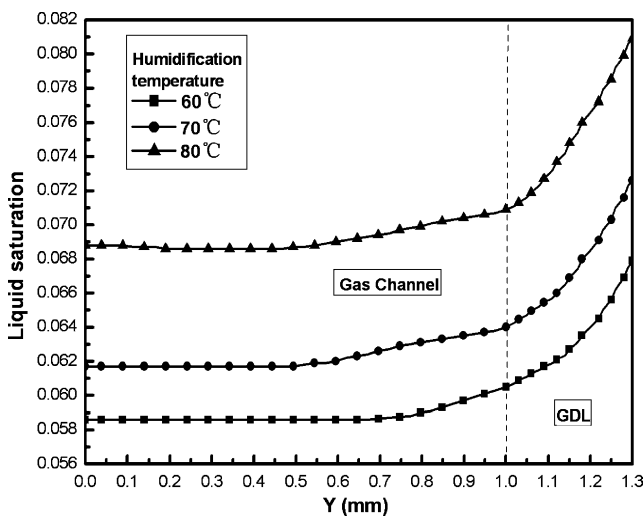

Fig. 14. Liquid saturation at $x = 22.36$ mm in the cathode channel and GDL at different humidification temperatures. The coordinate y starts at the channel wall (see Fig. 2). Case conditions: H_2 flow rate = 100 sccm, pressure on both sides = 3; air flow rate = 200 sccm, fuel cell temperature = 70 °C.
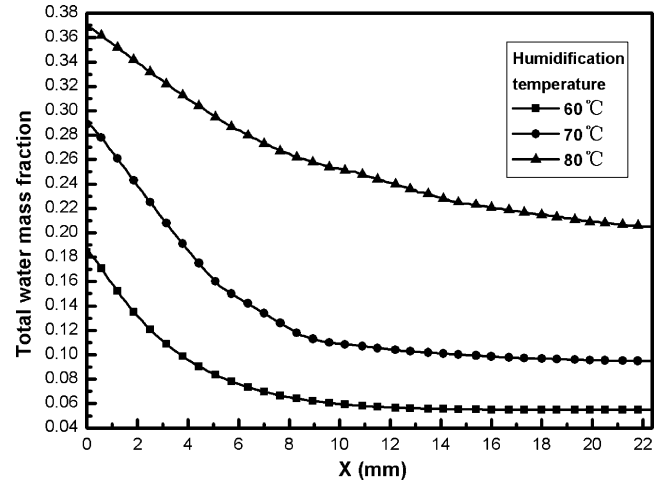

Fig. 15. Total water mass fractions at the interface of GDL and CL on the anode at different humidification temperatures. X represents the flow direction and $x = 0$ is the inlet (see Fig. 2). Case conditions: H_2 flow rate = 30 sccm, pressure = 3 atm on both sides; air flow rate = 120 sccm, fuel cell temperature = 80 °C.
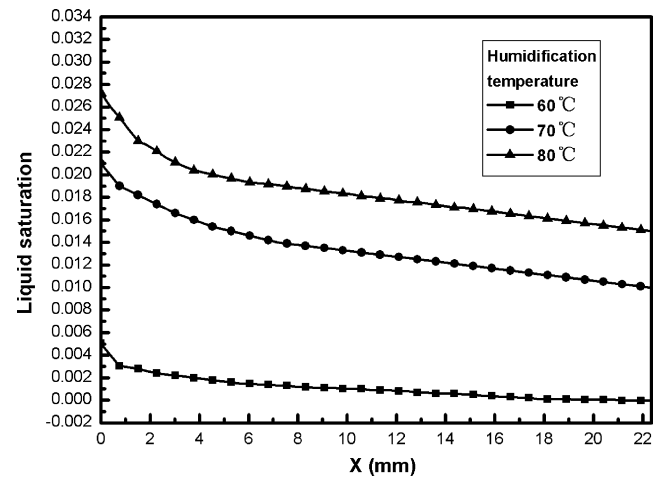

Fig. 16. Liquid saturation at the interface of GDL and CL at the anode at different humidification temperatures. The coordinate y starts at the channel wall (see Fig. 2). Case conditions: H_2 flow rate = 30 sccm, pressure = 3 atm on the both sides; air flow rate = 120 sccm, fuel cell temperature = 80 °C.

increases. This is due to the fact that, for each mole of hydrogen consumed, the net water transfer to the cathode side is less than one mole. It can also be seen from Fig. 15 that, the total water mass fraction is higher at higher gas humidification temperatures.

Fig. 16 shows the liquid water saturation in the anode catalyst layer at its interface with GDL. Liquid water increases along the anode flow direction due to hydrogen consumption as discussed above. Again, at higher humidification temperatures, liquid water saturation is higher.

5. Conclusion

A two-phase flow PEM fuel cell model is developed for the PEM fuel cell. The mixture two-phase flow model is used

in both the cathode and the anode, and it also used in the two gas channels in addition to the two GDLs and two catalyst layers. The modeling results at different operating conditions are compared with experimental data and good agreements are obtained. The model is used to study the effects of various operation parameters, and specifically the results of water distribution across different parts of a fuel cell are presented. The following conclusions can be obtained from this study. (a) In the cathode catalyst layer, total water mass fraction increases from its interface with the DGL to its interface with the catalyst layer. Within certain temperature range and sufficient gas stream humidification, total water mass fraction in the cathode catalyst layer and the membrane ionic conductance increases with fuel cell operating temperature due to the higher water generation rate. (b) The total water mass fraction in the cathode catalyst layer and the liquid volumetric fraction (liquid saturation) in the cathode channel and DGL increase with operating pressure due to higher water generation rate and lower vapor faction in the gas phase. (c) For counter-flow arrangement, generally, total mass fraction and liquid water volumetric fraction in the anode GDL and catalyst layer increases along the anode flow direction.

Acknowledgements

References

[1] D.M. Bernardi, M.W. Verbrugge, Mathematical model of a gas diffusion electrode bonded to a polymer electrolyte, AIChE J. 37 (1991) 1151–1163.

[2] D.M. Bernardi, M.W. Verbrugge, A mathematical model for the solid-polymer-electrode fuel cell, J. Electrochem. Soc. 139 (1992) 2477–2491.

[3] R.F. Hill, M.W. Verbrugge, Ion and solvent transport in ion-exchange membranes. II. A radiotracer study of the sulphuric. Nafion 117 system, J. Electrochem. Soc. 137 (1991) 893–899.

[4] T.E. Springer, M.S. Wilson, T.A. Zawodzinski, Modeling and experimental diagnostics in polymer electrolyte fuel cells, J. Electrochem. Soc. 140 (1993) 3513–3526.

[5] F.E. Springer, T.A. Zawodzinski, S. Gottesfeld, Polymer electrolyte fuel cell model, J. Electrochem. Soc. 138 (1991) 2334–2342.

[6] T.F. Fuller, J. Newman, Water and thermal management in solid-polymer-electrolyte fuel cells, J. Electrochem. Soc. 140 (1993) 1218–1225.

[7] T.V. Nguyen, R.E. White, A water and thermal management model for proton-exchange-membrane fuel cells, J. Electrochem. Soc. 140 (1993) 2178–2186.

[8] V. Gurau, H. Liu, S. Kakac, Two-dimensional model for proton exchange membrane fuel cells, AIChE J. 44 (1998) 2410–2422.

[9] T. Zhou, H. Liu, A general three-dimensional model for proton exchange membrane fuel cells, Int. J. Trans. Phenomena 3 (2001) 177–198.

[10] S. Um, C.Y. Wang, Three-dimensional analysis of transport and electrochemical reactions in polymer electrolyte fuel cells, J. Power Sources 125 (2004) 40–51.

[11] Z.H. Wang, C.Y. Wang, K.S. Chen, Two-phase flow and transport in the air cathode of proton exchange membrane fuel cells, J. Power Sources 94 (2001) 40–50.

[12] L. You, H. Liu, A two-phase flow and transport model for the cathode of PEM fuel cells, Int. J. Heat Mass Transf. 45 (2002) 2277–2287.

[13] L. You, H. Liu, A parametric study of the cathode catalyst layer of PEM fuel cells using a pseudo-homogeneous model, Int. J. Hydrogen Energy 26 (2001) 991–999.

[14] C.Y. Wang, P. Cheng, A multiphase mixture model for multiphase multi-component transport in capillary porous media. I. Model development, Int. J. Heat Mass Transf. 39 (1996) 3607–3618.

[15] P. Cheng, C.Y. Wang, A multiphase mixture model for multiphase multi-component transport in capillary porous media. II. Numerical simulation of the transport of organic compounds in the subsurface, Int. J. Heat Mass Transf. 39 (1996) 3619–3632.

[16] M.C. Leverett, Capillary behavior in porous solids, Tran. AIME 142 (1941) 151–169.

[17] A. Rowe, X. Li, Mathematical modeling of proton exchange membrane fuel cells, J. Power Sources 102 (2001) 82–96.

[18] K.R. Weisbrod, S.A. Grot, N. Vanderborgh, Through-the-electrode model of a proton exchange membrane fuel cell, in: S. Gottesfeld, (Ed.), Proceedings of the First International Symposium on Proton Conducting Membrane Fuel Cells, vol. 95–23, 1995, pp. 152–166.